

Ultraprecision machining of aberration-corrected diffractive optics with phase correcting groove trajectories

Marco Jagodzinski[✉],* Stefan Kühne[✉], and Dirk Oberschmidt
Berlin Institute of Technology, Institute of Machine Tools and Factory Management,
Micro and Precision Devices, Berlin, Germany

ABSTRACT. Spectroscopy has emerged as an essential technology, particularly in decentralized utilization within point-of-care devices. These applications demand compact, cost-effective designs with reduced complexity compared with traditional laboratory equipment. Achieving compactness often involves minimizing the number of components, necessitating that each remaining component fulfills multiple functions to optimize performance. However, this approach can lead to significant aberrations due to constructive compromises. Nevertheless, the known phase errors enable correction, often achieved directly through diffractive elements. Diffractive compensation of aberrations is commonly conducted through interference lithography, exploiting holographic techniques to produce gratings without explicit knowledge of the interference structure. Alternatively, mechanical manufacturing techniques offer the possibility of producing blazed gratings with greater efficiency. However, diffractive correction using mechanically fabricated gratings requires a precise understanding of individual groove trajectories, presenting an ongoing challenge. We employed ultraprecision (UP) mechanical manufacturing techniques to create aberration-corrected diffraction gratings for spectroscopic applications. To enable the machining of freeform trajectories, facilitating versatile fabrication of both planar and concave imaging blazed gratings, a modified five-axis UP machinery is employed. To correct the known wavefront errors of the exemplary use cases, a nonlinear phase function was applied and a numerical method was developed to derive trajectories from the phase errors and translate them into machine code. The use cases are a blazed imaging planar Littrow grating and concave Rowland gratings, showcasing corrected astigmatic wavefront deviation. The theoretical and experimental results are compared and discussed.

© The Authors. Published by SPIE under a Creative Commons Attribution 4.0 International License. Distribution or reproduction of this work in whole or in part requires full attribution of the original publication, including its DOI. [DOI: [10.1117/1.JOM.4.2.023501](https://doi.org/10.1117/1.JOM.4.2.023501)]

Keywords: diffractive optical elements; gratings; ultraprecision machining; diffractive optics

Paper 23040G received Dec. 24, 2023; revised Mar. 20, 2024; accepted Mar. 25, 2024; published Apr. 10, 2024.

1 Introduction

Various manufacturing processes coexist for the production of diffraction gratings. The coexistence arises due to different realizable structure dimension ranges, regarding the macroscopic dimensions (diameter, curvature) as well as the microscopic features such as groove spacing and sharpness of the blaze geometry. Each manufacturing process provides advantages and disadvantages in the common dimensional ranges, which depend on the application and have to be

*Address all correspondence to Marco Jagodzinski, m.jagodzinski@tu-berlin.de

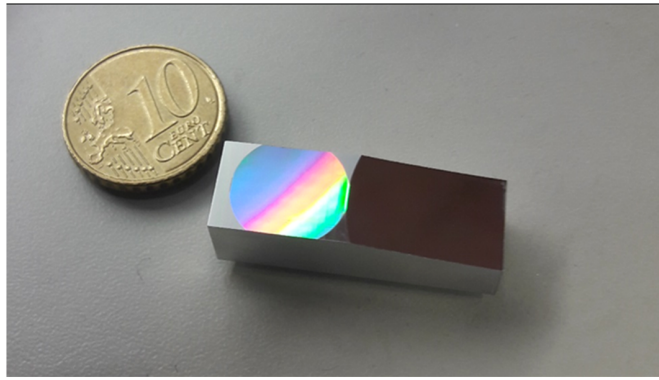


Fig. 1 Exemplary imaging blaze grating and concave mirror for a miniature spectrometer manufactured with UP technology. The curved grating and mirror were machined into an ultra-fine-grain aluminum alloy within one mounting, enabling precise relative positioning of the elements.

evaluated with respect to the individual case. The primary categorization involves lithographic and mechanical processes. Within the lithographic processes, further distinctions are made between direct writing and interference based methods.

The mechanical processes are subdivided into ruling and shaping processes and can be conducted on classical ruling engines as well as numerically controlled (NC) ultraprecision (UP) machine tools. The essential application-related criteria are the diffraction efficiency, the stray light, the imaging quality, and the f -number as well as the unit-related price and the unit-related delivery time. To combine diffractive and imaging properties, both principal methods are suitable for the realization of structures on curved surfaces. With such optical elements, compact spectrometer setups could benefit since optical elements and surfaces can be reduced. However, there is a risk of aberrations since the systems to be realized are often reflective setups in which an unfortunate angular illumination of the grating elements results due to the design. To correct these aberrations, the grating structures must be individually adapted to the setup. The resulting grating grooves are therefore neither equidistant nor parallel and must be curved by means of machining with kinematics in multiple degrees of freedom (DOF).

A significant advantage of lithographic production is that the local groove shape does not have to be explicitly calculated, as it results from the interference pattern from the holographic setup. With regard to the mechanical processes, the trajectory of each groove must be known. Especially for UP machine tools, an explicit description in the form of a set of tool path coordinates is needed. For this approach, a calculation basis is needed that can determine the trajectories of the grating grooves and convert them into NC machine code. With the presented method, this can be realized for the first time, and the application-specific advantages of UP gratings (exemplary depicted in Fig. 1) in their respective application can be used for aberration-corrected systems as well.

2 UP Machining of Diffraction Gratings

The advantages and disadvantages of mechanical or lithographic manufacturing are diverse and highly dependent on the application. The significant advantage of interference-lithographic manufacturing is superior ghost suppression, whereas mechanical processes allow for asymmetric blaze structures across a wide range of dimensions, potentially leading to higher efficiencies.

The lithographic fabrication of aberration-corrected gratings, specifically concave aberration-corrected gratings made by interference lithography (IFL), is described very comprehensively by Glaser.¹ The possibilities and limitations of lithographic manufacturing of blaze gratings are also explained, with reference to the alternative of UP machining. The review indicated that there were no known UP technologies that have actually fabricated aberration-corrected gratings. To the best knowledge of the authors, this is still state of the art. Thus, the work presented here is the first one that deals with the UP machining of this type of gratings.

It has been demonstrated many times that the UP technology is suitable for manufacturing high-quality grating structures. The oldest methods of grating production are so-called ruling

machines, which produce the grating through plastic surface deformation. Since this technology can produce gratings more suitable for some applications than IFL, it is established today, and there have also been attempts in the history of development to realize more DOF so that the method is not limited to planar gratings. The manufacturing of curved diffractive optical elements (DOEs) therefore is theoretically feasible using traditional ruling machine tools. However, this is only achievable for very large radii of curvature, making it unsuitable for compact optical systems. A patented method and specified grating cutting machine developed by Harada and Kita² and Harada et al.³ have addressed the challenge of producing strongly curved optics. This method combines the principles of classical ruling machines with a specialized guidance system adapted to the curvature of the grating. It should be noted that this approach cannot adjust the blaze angle to match the local surface and that it lacks flexibility with respect to variations in groove spacing and curvature. This is because of the limited DOF that are needed for diffractive aberration correction.

These DOF are provided by UP machine tools⁴ nowadays. Building upon experiences with continuous optics, the application of UP technologies has gained recognition for noncontinuous optical structures.⁵ Gläbe and Riemer⁶ and Brinksmeier et al.⁷ underscored the potential when transitioning to discontinuous optical structures, with a particular emphasis on their importance in developing replication masters for micromirror arrays, multiprisms, and DOE.

Different technologies, such as fast tool servo,^{8,9} microchiseling,^{10,11} shaping,¹² turning,¹³ and fly-cutting,⁵ are used to manufacture optical discontinuous structures. However, to achieve the necessary precision in the single-digit nanometer range, for DOE, it is important to further minimize the influence of sources of disturbance, e.g., vibration and temperature. Even for comparatively large structures in the micrometer range, temperature management is considered a critical factor for the achievable optical performance of cyclic structures such as lighting units.¹⁴

By minimizing disturbances, the production of planar blaze gratings by means of UP cutting processes became well-established. The precise manufacturing of those gratings by ruling or cutting with diamond tools was already implemented on traditional ruling machines. Kühne et al.¹² detailed the adaptation of these processes to UP systems to enable the availability of multiple DOF and points to the future potential for aberration correction.

As previously mentioned, there are various approaches to machine planar and nonplanar diffractive optics that incorporate refractive or reflective imaging. One method for manufacturing nonplanar gratings involves a modified fly-cutting process, where a fly-cutter is moved along sagittal trajectories. The overlap of the interrupted cuts results in individual grooves, but the process introduces a standard deviation of over 50 nm in groove positions. This method also yields a surface roughness of $R_q = 14$ nm.¹⁵ A drawback is the required relatively slow feed rate $f_x = 40$ mm/min to minimize overlap between individual cuts, leading to a repetitive surface structure. Another unconventional manufacturing approach is the turning of imaging gratings, as demonstrated by Gebhardt et al.¹³ regarding an Offner configuration for MERTIS. This convex grating has a pitch of 11 mm^{-1} ($g = 90.9 \text{ } \mu\text{m}$) and a roughness $R_q = 7$ nm. A benefit over the fly-cutting method is that each grating groove is created by a single cut. However, this method is limited to optics with rotational symmetry, and the optic radius is fixed by design, preventing the full utilization of DOF for blaze angle tracking. Moriya et al.¹⁶ and Takeuchi et al.¹⁷ developed an extension of DOF to achieve six-axis simultaneous motion for microgrooving curved surfaces with individually shaped grooves. Yet, multi-axis setups face resolution limitations due to the high number of axes involved. In response, Kühne et al.¹² proposed reducing the number of axes to the minimum required to optimize the fabrication of metrological DOEs. Kühne¹⁸ presented the full utilization of the DOF of UP machine tools for the production of blaze gratings as well as methods that compensate for the resulting inaccuracies with the increasing number of axes involved. Since the interaction between DOF and inaccuracies with regard to the optics and their application have a nontrivial relationship, Jagodzynski¹⁹ presented methods to determine the application-related consensus between the necessary DOF and the highest possible optical performance.

However, most of the existing works are limited to equidistant grating structures or merely highlight the potentials of nonequidistant structures but are not capable of calculating the corresponding structures and transferring them into production. Imaging only results from the curvature of the optics; diffractive possibilities remain unused. Hence, aberration corrections have

not been feasible from a technical standpoint thus far. To overcome this limit, an application-specific number of DOF and models for trajectory calculation are required. The resulting calculation methods for utilizing diffractive aberration correction, which enable the production of highly efficient blaze gratings, thus further expanding upon the existing advantages of mechanical manufacturing by incorporating aberration correction, are part of this paper. These methods are based on the calculation and manufacturing of free-form trajectories.

3 Experimental Setup

For the manufacturing of the experimental diffraction gratings, a UP machining center MMC1100 from LT ULTRA-PRECISION TECHNOLOGY GMBH, Herdwangen-Schönach, Germany, was used. To meet the nanoscale requirements and reduce mechanical and thermal disturbances, the machine underwent several modifications.¹⁸ The machine tool is shown in Fig. 2.

The three-axis machine kinematics have been extended by a tilt-rotate module with two serial rotary axes. The control system enables the simultaneous actuation of five axes. To maintain thermal stability ($\Delta T = 30$ mK), a custom-developed air–water temperature control unit and machine enclosure was implemented. Vibration suppression is achieved through an actively leveled vibration damping system, mechanically decoupled control cabinet, and portal reinforcement with separate granite plates. The technical specifications of the machine tool are shown in Table 1.

3.1 Machining Process

The machining of diffraction gratings can be conducted using the described machine tool through both ruling and shaping processes. Extensive research on ruling and shaping processes, along with parameters for both methods, is provided by Refs. 18 and 20. However, it is worth noting that the ruling process, especially when applied to curved geometries, is considered significantly more delicate than shaping processes due to its complexity and sensitivity. Variations of the

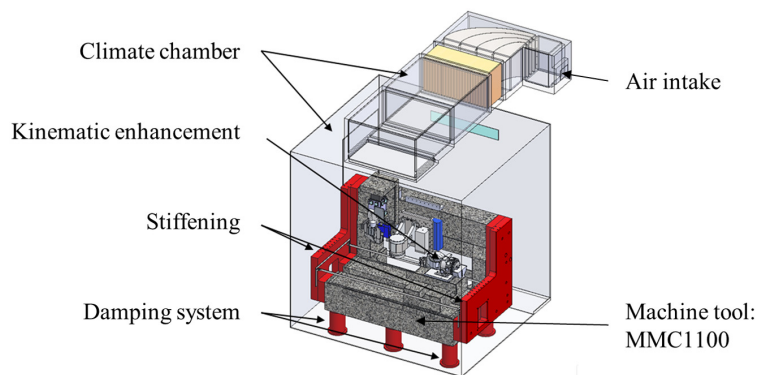


Fig. 2 Computer aided design (CAD) visualization of the modified UP machine tool utilized to manufacture the experimental diffraction gratings.

Table 1 Technical specifications of the experimental machine setting.

Frame, bearings	Natural granite, hydrostatic bearings (all axes)		
NC control	DELTA TAU Turbo PMAC		
Axes travel range	X, Y, Z: 1100, 200, and 170 mm		
Lateral accuracy over travel range	100 nm/100 mm		
Positioning resolution	X, Z: 25 nm		A: 5"
	Y: 1 nm		C: 3"
Temperature stability	$\Delta T: \pm 0.03$ K ¹⁸		

process force may cause deviations in groove geometry, leading to losses in optical performance. Therefore, applying a constant force normal to the grating surface is crucial for groove quality, which is achieved by weights, mounted to the tool-guidance mechanics. In addition, the tool engagement point is located tangentially on the edge of keel-shaped or cylindrical tools. Assuming multi-axis relative movements of the tool or workpiece, this leads to variations in the tool engagement point and/or resulting normal process force. Therefore, as mentioned earlier, ruling processes are only feasible for slight curvatures and/or groove width variations.

By contrast, shaping processes have an almost singular tool engagement point, making them suitable for multi-axis machining of curved metal grating masters. Machining using shaping on curved geometries is described for Ni–P, and Au and suitable machining parameters have also been identified for rapid solidified aluminum alloys.²¹ Surface roughness compensation is a current research topic, and approaches to reduce the surface roughness of the used aluminum alloy using ion beam processing are described in Ref. 22.

The process parameters and strategies for tool setup and alignment are derived from Refs. 18 and 20. The grooves are produced on premilled blanks, which are glued to a chuck on the machine tool. The grating surface processed in the shaping process was preprocessed using fly-cutting or diamond radius milling. The axis orientation of the grating elements in this paper matches the experimental machine setup shown in Fig. 3. To achieve the best results and ensure a constant chip thickness, the cutting process is carried out in a precut (roughing) and a finishing cut.

3.2 Process Kinematics

Similar to traditional ruling machines, the manufacture of diffraction gratings using UP machining requires the use of machine tools with at least two translational axes. One axis is used for the longitudinal cutting motion of the tool (the fast axis), while multiple grooves are created by laterally offsetting the tool along a slow axis. For roughing and finishing strategies, the feed and chip thickness adjustments take place along the feed axis.

For the manufacture of curved gratings, at least three axes are required. The cutting motion along the grooves can be carried out by a rotary axis, as is often found in UP lathes.²³ Alternatively, the cutting motion can also be achieved by simultaneous actuation of the X and

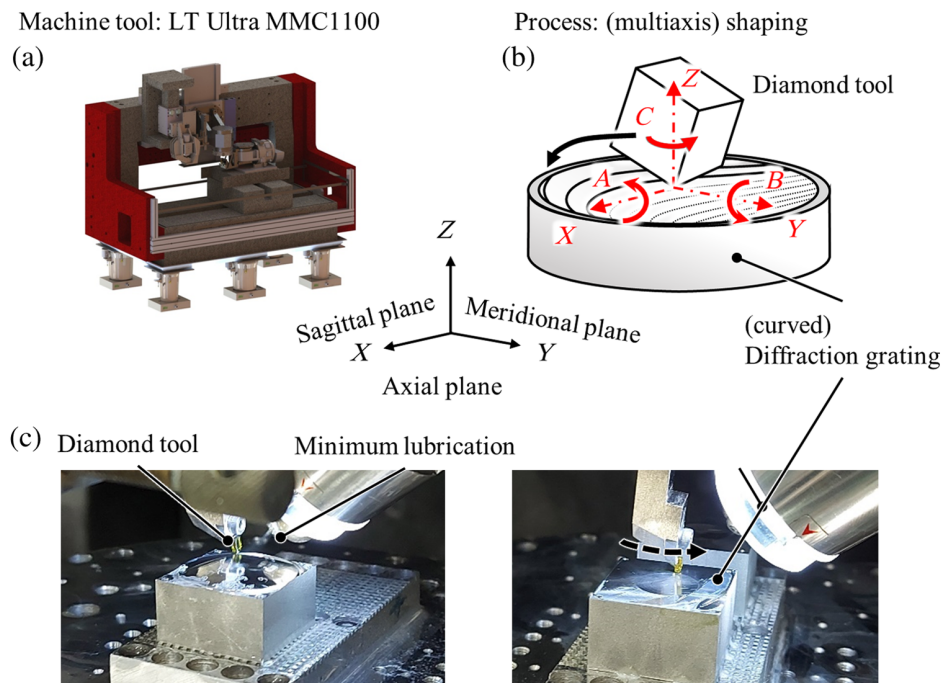


Fig. 3 Depiction of the employed machining configuration.¹⁹ (a) CAD image of the used machine tool. (b) Sketch of (exaggerated) motion and coordinate system of the process. (c) In-process photos of grating manufacture.

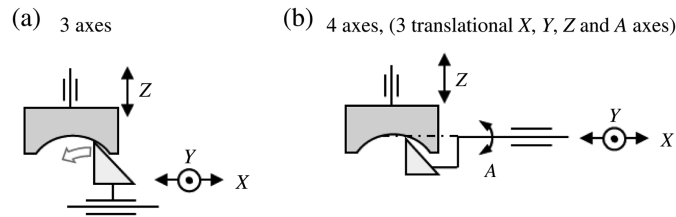


Fig. 4 (a) Used kinematic configuration within this paper. The tool is guided with only translational cutting motions. (b) Possible configuration, described in Refs. 18 and 19. The tool is mounted coaxially to the rotational a axis.

Z axes, which is common in UP milling machines as used in this paper. Therefore, the experimental gratings were solely machined by (simultaneous) translational cutting motions, as depicted in Fig. 4.

For equidistant grooves without Z -axis curvature, both the fast and feed axes must be actuated simultaneously. For grooves with axial curvature, the slow axis also needs to be engaged in simultaneous motion. While the described machine tool is capable of up to five-axis simultaneous motion, a three-axis motion strategy was employed for the gratings in this study. However, if rotational alignments of the tool are necessary, additional rotational axes can be used. This setup, depicted in Fig. 4, permits four-axis manufacture, allowing the blaze angle to be guided tangentially to the surface of the grating.¹⁸

4 Aberration-Corrected Blazed Gratings

4.1 Description of Exemplary Concave Grating Mount

In dependence of the optical configuration, low f -numbers, low radii of curvature R , and high angles of incidence tend to increase wavefront errors of reflective dispersion spectroscopes, which reduce the imaging quality. The reduction, or correction, of the wavefront errors can, at least partially, be achieved by the choice or design of the optical arrangement if enough DOF are available. An example is the use of aspherical grating elements or exploiting specific symmetries or proportions within the topology of the spectrometer components. Diffraction gratings typically introduce a linear phase shift into the reflected or transmitted wavefront within the meridional plane of the mount which correlates with equidistant, linear groove trajectories. A wavelength-dependent imaging effect can be achieved if a nonlinear phase shift is introduced into the diffracted wavefront. This can be used to correct wavefront errors and/or achieve an imaging functionality at all for the diffracted beam. The phase shift is defined by the phase function of the grating and is typically determined by analytical or numerical methods.

Based on the phase function, the diffractive structure must be calculated and transformed into computerized numerical control trajectories. The phase shift is described spatially by the phase function Φ_{gr} of the grating. Modifying the phase function enables another DOF, enabling wavefront correction. The phase function must not be necessarily calculated directly, as a foundational series of papers by Noda et al.^{24–26} enabled the determination of optical/imaging properties of concave gratings from the interference-lithographic parameters. However, due to advancements in computing technology and related software, the optical design is conducted predominantly by ray tracing techniques, as done within this paper. The theoretical investigations of the imaging properties carried out here were performed with Zemax OpticStudio, in which the phase function is enabled by “binary 1” elements. With these, the phase function Φ_{gr} of the grating is described by a two-dimensional (2D) polynomial

$$\Phi_{\text{gr}}(x, y) = m \cdot \sum_i \sum_j C_{ij} x^i y^j. \quad (1)$$

By adjusting the polynomial coefficients C_{ij} , a location and spatial direction-related phase shift into the wavefront is made possible. This phase function is closely related to the existing optical errors to be corrected. Nonlinear phase functions can lead to nonlinear trajectories and/or variations in groove density. Therefore, the evaluation of the mechanical manufacturing aspects requires a quantification of the phase functions as well as the corresponding wavefront errors.

In the presented work, the existing optical errors and the phase function of the grating are quantitatively assessed using a concave Rowland grating mount as an example. The selected design is a concave echelette grating mount with a radius of curvature $R = 75$ mm and a groove width $b = 3$ μm . A raytrace of the mount is depicted in Fig. 5. As is typical for Rowland mounts, the nonzero angle of incidence toward the curved surface of the concave grating results in an astigmatic wavefront deviation, which is visible in the spot diagrams of the uncorrected grating in the middle section of Fig. 5.

In the meridional plane, the spectrum is imaged or focused on the Rowland circle. By placing the detector tangentially on the Rowland circle, a distance with optimized or lowest possible spectral blur can be found. This arrangement provides the advantage of minimized meridional coma so that, over the considered wavelength range, an almost homogeneous meridional width of the spectral images, and thus spectral resolution, is achieved. However, a nonnegligible amount of dispersed light is lost due to the finite height of available photodetectors.

The correction of this error can be applied by a variable-line-space grating in which the astigmatism is corrected in the meridional plane. This is applied for interference-lithographic gratings as well as classically ruled gratings with linear but nonequidistant groove width. However, it leads to a nonorthogonal illumination of the detector. In this paper, an orthogonal illuminance approach is adopted in which the sagittal components of the wavefront error are spectrally corrected. By application of a sagittal component of the phase function, a significant reduction of astigmatic wavefront distortion can be achieved, which approaches the diffraction limit for one specific wavelength. This improvement can be seen in the lower-middle section of Fig. 5, where there is a noticeable decrease in the vertical extent of the spot diagrams. A close-up of the spectral spot images, which comply with the pixel size of state-of-the-art detectors, is

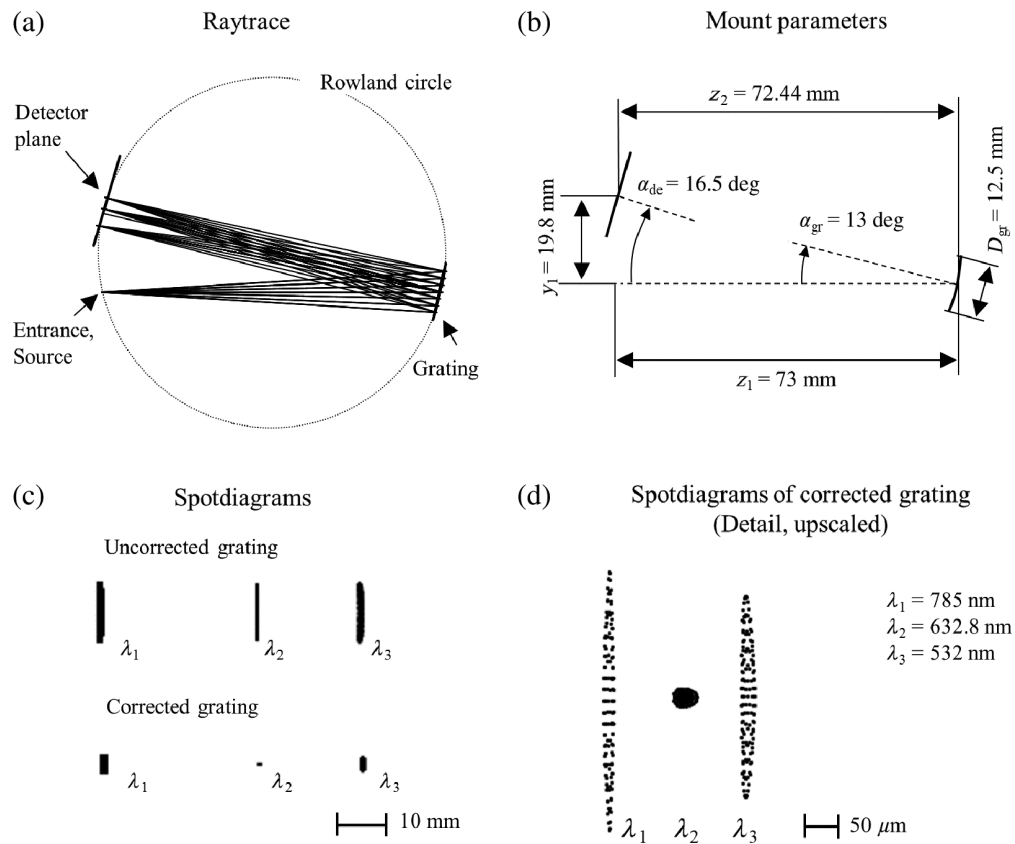


Fig. 5 Raytrace and spot diagrams of an exemplary concave grating mount.¹⁹ (a) Drawing, including raytraces of the exemplary Rowland mount. (b) Geometrical parameters of the mount. (c) Comparison of spot diagrams of uncorrected (top) and corrected (bottom) concave diffraction gratings. (d) Detailed image of corrected spot diagrams of the corrected grating. The lateral distance between spot diagrams for each wavelength was shortened to fit into the figure.

depicted in the right section of the figure. Assuming an application within the visible light spectral range, a spectral bandwidth of 400 to 800 nm is suggested, if no order sorting filters are applied. The parameters and coefficients for the corrected Rowland grating are listed in Table 2.

4.2 Phase Function for Correction of Wavefront Error

Despite the low angle of incidence on the curved surface, astigmatic wavefront disturbances are clearly recognizable. Due to the occurrence of aberrations of the concave grating, the arrangement is investigated with respect to the magnitude and composition of the wavefront disturbances. For the presented mount, a representation of the wavefront errors by the Zernike polynomials in fringe convention has been chosen (“piston” corresponds to Z_1). The values of the individual Zernike polynomials in the detector plane are depicted in Fig. 6. Highest values are found for the Z_5 polynomial, which corresponds to astigmatism. As the detector is shifted toward the meridional focus, the spherical and piston take nonzero values. There is an occurrence of higher order aberrations, but those are below the Z_5 polynomial, so astigmatism takes by far the largest portion of wavefront distortion.

Correction of the wavefront errors, especially Z_5 -correlated astigmatism, can be achieved using a nonlinear phase function. In Zemax OpticStudio, this is accomplished using binary 1 elements as diffractive surface elements. These elements allow for the introduction of a

Table 2 Parameters of the Rowland mount and grating.¹⁹

Parameter	Symbol	Value
Rowland mount parameters		
Radius Rowland circle	R	75 mm
Design wavelengths		
Minimum wavelength	λ_1	532 nm
Central wavelength	λ_2	632.8 nm
Maximum wavelength	λ_3	785 nm
Spectral bandwidth (suggested)	$\Delta\lambda$	400 to 800 nm
Diffraction order	m	1
Geometrical parameters of Rowland mount		
Distance entrance—grating	z_1	73.0 mm
Distance grating—detector plane	z_1	72.44 mm
Vertical distance entrance—detector plane	y_1	19.81 mm
Grating tilt angle	α_{gr}	13 deg
Detector plane tilt angle	α_{de}	16.5 deg
Grating parameters		
Grating diameter	D_{gr}	12.5 mm
Blaze angle	α_{bl}	6 deg
Average groove period	B	3 μm
Resolving power	P_r	4156
Working f -number	K	6.22
Coefficients for corrected grating		
	C_{01}	2094 mm^{-1}
	C_{20}	3.496 mm^{-2}
	C_{02}	-0.172 mm^{-2}

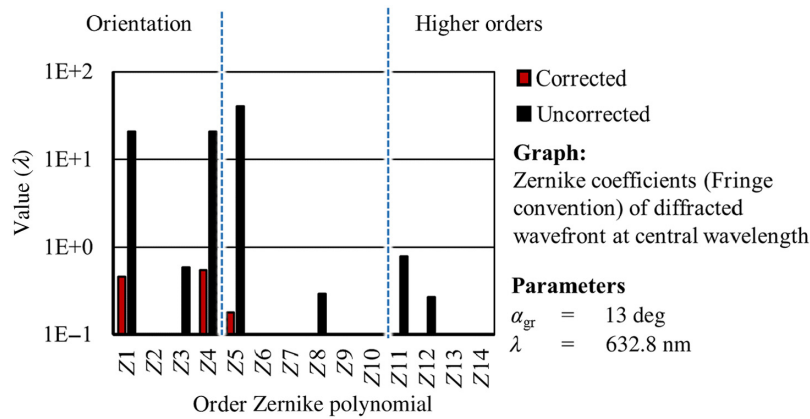


Fig. 6 Coefficients of Zernike polynomials of diffracted wavefront for corrected and uncorrected concave gratings.¹⁹

wavelength location-dependent phase shift into the transmitted or reflected wavefront, defined by a multidimensional polynomial. In some cases, the polynomial coefficients C_{XX} correlate to optical effects, for example, the inclusion of nonzero C_{01} coefficient causes a linear, location-dependent phase shift, which corresponds to the optical dispersion of a classical diffraction grating with equidistant linear groove pattern. More complex diffractive effects can be achieved through the inclusion of higher dimensional polynomial terms into the phase function. In the case of the presented optical mount, nonzero C_{20} and C_{02} coefficients enable the compensation of the astigmatism-dominated wavefront error. Through optimization, an root mean square (RMS) wavefront error below 0.27λ is achieved for the central wavelength on the detector plane.

4.3 Calculation of Trajectories

The qualitative effect of a nonlinear phase function is illustrated in Fig. 7. In dependence of the aspired optical functionality, the phase function exhibits a nonlinear curvature so that nonlinear and/or nonequidistant groove trajectories are to be expected. Unlike interference-lithographic gratings, which require a corresponding holographic setup for the binary 1 surface, the intended manufacture via diamond shaping eliminates this need. A quantitative description of the groove trajectories is fundamental for machine programming, which can be determined from the phase function. Since each groove corresponds to an integer 2π -phase shift of the wavefront, the groove trajectories can be determined by wrapping the phase function with a 2π modulus. Therefore, the identification of 2π -shifts enables the determination of groove trajectories, which are described by the x and y coordinates.

The identification of 2π -shift coordinates can be achieved analytically by finding the inverse of the phase function, allowing for direct calculation of x and y coordinates. In the case of a polynomial phase function, for each groove n , the zeros of $\Phi_{gr} = n \cdot \pi$ need to be found, which is trivial for linear or quadratic expressions, but may become challenging for higher order polynomials. Therefore, a numeric approach for the groove coordinate identification is pursued and presented in which the grating surface is scanned in the X and Y directions for two shifts of the phase function. Each groove is segmented into a set of coordinates that need to be traced during the machining process. As it is assumed that the groove pattern is mainly lamellar with trajectories only following slightly curved paths, a segmentation of the trajectories along the x axis of the grating is applied. The segmentation distance Δx is chosen in the dependence of the command rate of the machine numerical control and groove trajectory curvature. A segmentation distance of $\Delta x = 20 \mu\text{m}$ was selected as this suffices the command rate of the machine control. In addition, this segmentation distance corresponds to lateral positioning deviations between the theoretical grating groove and the linear interpolated tool path well below 1 nm for the presented scenario. By identifying the y coordinates for each groove at an integer multiple segment of Δx , a full quantitative description of each groove is achieved. For the determination of the y coordinates, a scanning algorithm with search distance $\Delta y = 1 \text{ nm}$ was implemented, which identifies 2π -phase shifts at integer multiples of Δx . The relation between found coordinates

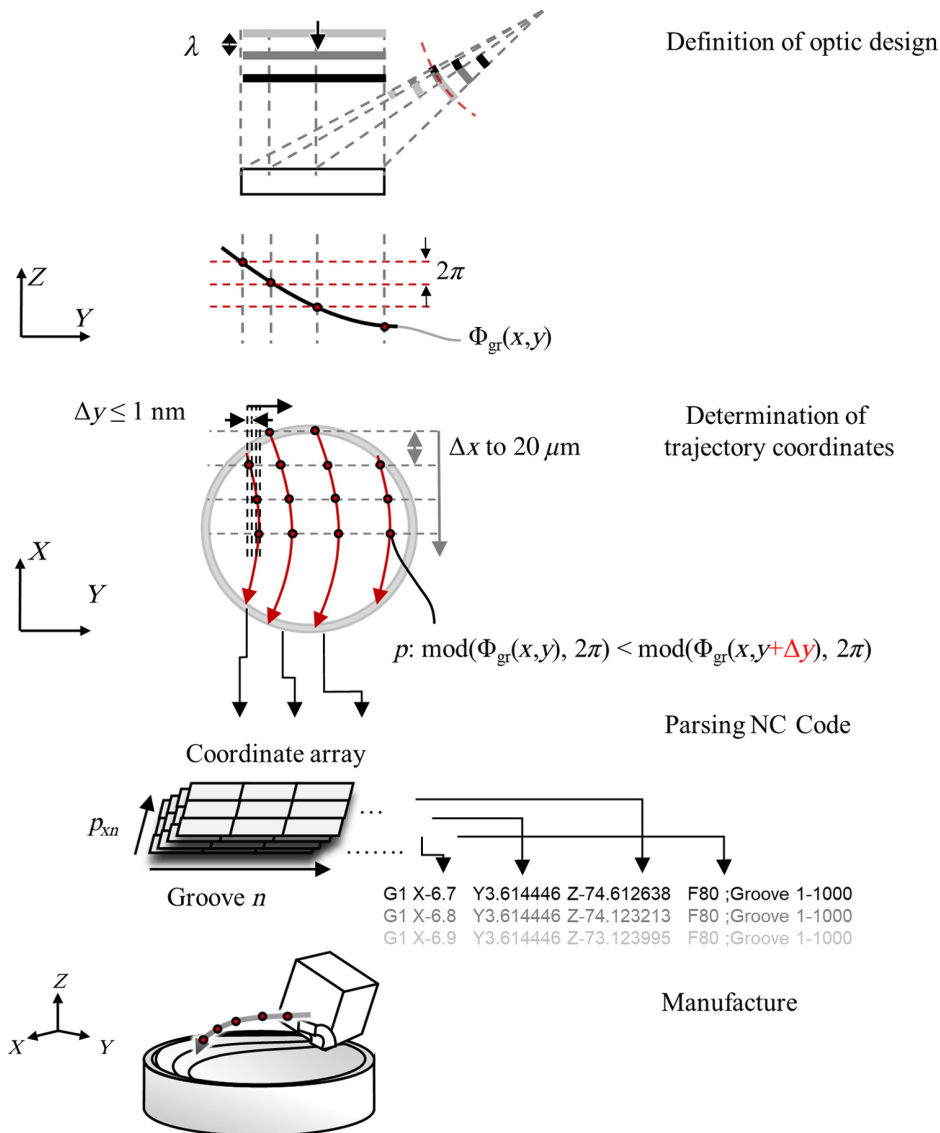


Fig. 7 Schematic representation of the numerical computation of machine trajectories.¹⁹ A phase function Φ_{gr} (typically determined by numerical tools) is segmented into specific trajectory coordinates, where 2π -phase shifts occur and then parsed into an NC machine code.

p and individual grooves is determined through the integer share modulus of the phase function. The z coordinates are calculated analytically based on the surface description of the element or grating, in this case, a spherical surface. The coordinates of the trajectories are stored in arrays indexed by the infeed j and groove number n . The conversion into NC code is conducted by two counting loops using the parsing logic shown in Fig. 7.

4.4 Implications of Diffractive Aberration Correction on Machining Kinematics

The grooves of the presented grating follow a nonlinear shape due to the inclusion of a nonzero, nonlinear coefficient in the sagittal direction of the phase function. Thus, the grooves—and corresponding trajectories of the diamond tool—are curved in the axial plane of the grating. State-of-the-art diamond cutting tools have a nonzero side clearance angle α_p , which is usually in the range $3 \text{ deg} < \alpha_p < 10 \text{ deg}$. Higher values severely weaken the tool, which makes it more susceptible to wear and damage to the cutting edge. This must be considered in the manufacture of grooves with curvature in the axial plane. If the local angle of the groove trajectory γ_{traj} exceeds the side clearance angle α_p [see Fig. 8(a)], the flank of the tool contacts the cut groove, which causes unwanted deformation and damage to the grating as well as the cutting tool, as depicted in

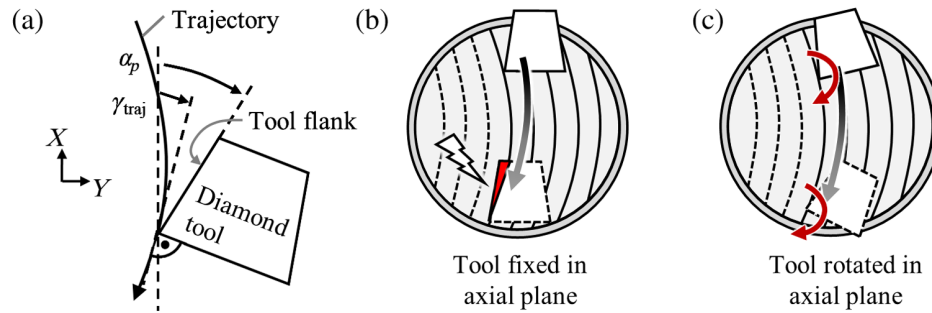


Fig. 8 (a) Tool angles in the axial plane, (b) potential groove damage without tool rotation in the axial plane (schematic), and (c) tool rotation in the axial plane (schematic).¹⁹

Fig. 8(b). State-of-the-art UP machine tools can potentially circumvent this kind of flank damage by rotational guidance of the diamond tool, as depicted in Fig. 8(c). However, the introduction of an additional rotational axis in the manufacturing process increases the complexity of setting up the machine tool and reduces the achievable positional precision of the grooves. Due to the finite precision of axis bearings, motors, measurement systems, and NC control, systematic and random tool positioning errors are introduced into the cutting process, which cause groove positioning errors and thus an elevation of the stray light level of the grating. Therefore, unless axial groove damage prevention is absolutely necessary, it is preferred to maintain axial fixation of the tool.

To assess the need for additional axial tool rotation, the angles of the groove trajectories need to be determined. As the groove trajectories are defined by the phase function of the grating, the local angle of the groove corresponds to the local gradient of the phase function within the axial plane. Therefore, according to Eq. (2), the arctangent of the quotient of the partial derivatives of the phase function equals the local angle of the groove trajectories

$$\gamma_{\text{traj}} = \tan^{-1} \left(\frac{\frac{d\Phi_{\text{gr}}}{dx}}{\frac{d\Phi_{\text{gr}}}{dy}} \right). \quad (2)$$

Thus, a tool rotation is not necessitated, if the local groove trajectory angle is below or equal the side clearance angle α_p of the tool for every section of the grating surface S_{gr}

$$\alpha_p \geq \tan^{-1} \left(\frac{\frac{d\Phi_{\text{gr}}(x,y)}{dx}}{\frac{d\Phi_{\text{gr}}(x,y)}{dy}} \right) \quad \forall x, y \in S_{\text{gr}}. \quad (3)$$

This implies that the tool parameters and machining settings depend on the optical parameters of the grating and setup. In Fig. 9, the maximum trajectory angles for various grating tilt angles and

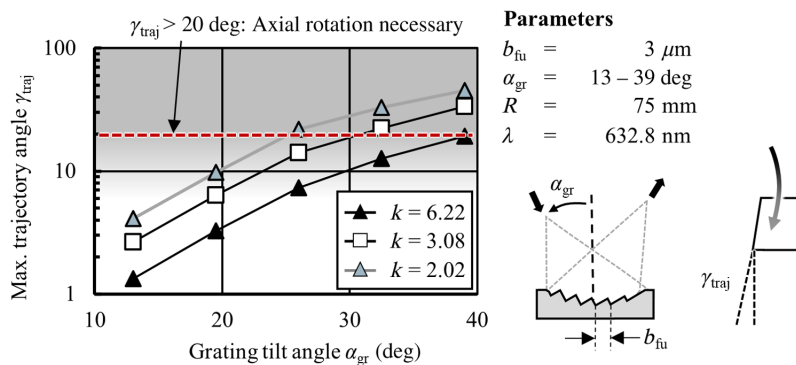


Fig. 9 Maximum angle of the trajectories in dependence of the angle of incidence and f -number.¹⁹ Due to cutting tool stability, a trajectory angle γ_{traj} above 20 deg is considered the upper limit of manufacturable gratings with only translational tool guidance. Scenarios with γ_{traj} above 20 deg (higher grating tilt angles and/or low f -numbers) demand a rotational axis within the cutting process).

f -numbers k for the selected Rowland mount setup are depicted. Lower f -numbers and higher grating tilt angles lead to increased aberrations, necessitating larger coefficients C_{20} and resulting in steeper trajectory angles γ_{traj} for full astigmatic aberration correction for the central wavelength. Therefore, to enable rotational-free manufacturing, a compromise in mount design regarding grating tilt angle and f -number must be achieved.

5 Results

Planar and concave curved diffraction gratings were manufactured and examined to demonstrate the findings described in Secs. 4.1–4.3. The results are presented in Sec. 5 and demonstrate the achievable imaging capabilities of diamond machined diffraction gratings.

5.1 Planar Imaging Grating

Imaging functionalities can be demonstrated with flat gratings. Typically, flat gratings comprise equidistant grooves and a linear phase function (nonzero values for only C_{01} coefficient). However, an assessment of the imaging diffractive properties requires far less effort for planar gratings, as the qualification of planar wavefronts is far less dependent on the spatial positioning of the grating and detecting elements. In addition, compared with curved optics, manufacturing complexity requires less effort, as the machine tool only needs to be set up in 3 DOF (Z distance of the tool, sagittal, and meridional rotation of grating sample). Therefore, a flat grating design with focusing capabilities was designed using Zemax OpticStudio and manufactured via three-axis diamond machining. In Fig. 10(a), a flat sample with two experimental flat gratings ($F1$ and $F2$) is depicted. Grating $F1$ corresponds to classical equidistant-groove gratings. The C_{01} coefficient of grating $F1$ is 1570 mm^{-1} , which corresponds to a groove period $b = 4.002 \mu\text{m}$

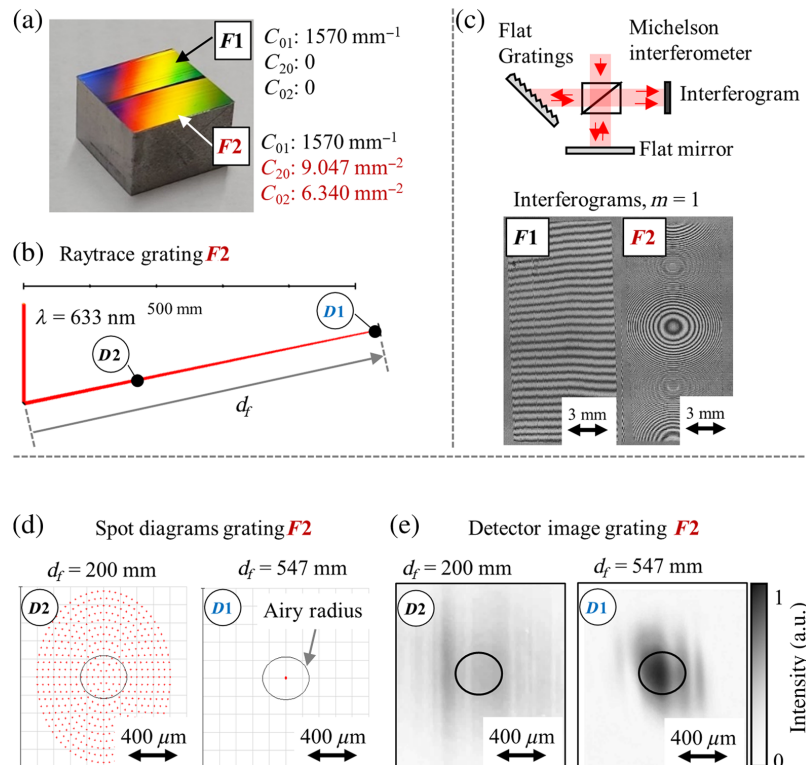


Fig. 10 (a) Experimental flat gratings, with ($F2$) and without ($F1$) imaging phase function.²⁷ (b) Raytrace of the imaging grating $F2$. The grating enables to focus the first diffraction order of a HeNe laser beam. The diffracted beam was probed in two locations ($D1$, focused; $D2$, defocused). (c) Interferometric testing of the flat gratings under the first order (Littrow condition). The circular interference pattern for grating $F2$ clearly depicts the nonplanar wavefront of the diffracted light. (d) Spot diagrams of grating $F2$ of the probing locations $D1$ and $D2$. (e) CMOS detector images of the probing locations, clearly depicting a focus on the beam at the designed distance.

($2\pi/1570 \text{ mm}^{-1} = 4.002 \mu\text{m}$). Grating $F2$ comprises two nonzero coefficients C_{20} and C_{02} which were obtained by optimizing those two parameters toward minimal focal spot size. When illuminated with a collimated HeNe laser beam at an angle of incidence of 45 deg, the element achieves a focusing capability at $df = 547 \text{ mm}$, as depicted in Fig. 10(b). Both gratings were machined using the same machine tool, diamond tool, and bulk sample, ensuring that they only differ in phase function and groove trajectories.

Testing with interferometry is straightforward due to the flat geometry of the gratings. For the wavefront assessment of gratings $F1$ and $F2$, a Michelson setup with a flat reference mirror, as depicted in Fig. 10(c), was used in the first-order autocollimation (Littrow mount). For grating $F1$ straight, equidistant interference fringes are observed so that the reflected, diffracted wavefront is of planar shape. By contrast, ellipsoid interference fringes are observed for grating $F2$ in nonzero diffraction orders. As depicted in Fig. 10(d), a ray analysis via spot diagrams predicts a near diffraction limit focusing at a focal length of $d_f = 547 \text{ mm}$. Assuming an RMS diameter of 1.1 mm for the testing laser beam, an Airy radius of ca. $128 \mu\text{m}$ can theoretically be achieved. This is caused by the relatively long focal distance and small diameter of the testing laser beam. Yet, a focusing functionality can be observed experimentally using a 2-dimensional complementary metal-oxide-semiconductor (2D CMOS) sensor. The detector images for the focal and an intermediate distance are depicted in Fig. 10(e). Maximum intensity is observed within the illustrated Airy disc in the lower right image in Fig. 10(e), which corresponds to the expected image, as the raytracing simulation does not account for the spatial intensity distribution near the diffraction limit of the setup. An intensity distribution slightly outside the Airy radius is to be expected for a real measurement due to the finite precision of detector positioning as well as the finite beam quality of the source. Thus, imaging functionality for planar diffractive elements, as depicted, can be achieved. However, it shall be emphasized that the imaging effects of nonzero coefficients C_{0X} and C_{X0} are dependent on diffraction order and wavelength. This results in strong focal shifts for varying wavelengths, which complicates the use in dispersive spectrometer setups but could potentially be of use for chromatic aberration correction in off-axis systems, analogous to hybrid lenses in on-axis mounts.²⁸

5.2 Concave Imaging Grating

The Rowland grating, described in Sec. 4.1, was manufactured by means of diamond machining, as shown in Fig. 11(a). Analogous to the previously described flat sample, a concave curved sample with linear ($G1$) and nonlinear ($G2$) phase-function gratings was manufactured. Both gratings are situated on the same curved surface with $R = 75 \text{ mm}$ and a total diameter of 12.5 mm. The sample is diametrically divided so that each grating is divided into one half of the sample, as illustrated by the dashed line in Fig. 11(a).

Testing the imaging properties involved imaging the diffracted beam from an incident light source in the designed Rowland mount. For the depicted results, a red light emitting diode (LED) (630 nm) and HeNe laser, illuminating a $300\text{-}\mu\text{m}$ pinhole, were used. Using a shutter to cut off one half of the diffracted beam, as it is illustrated in Fig. 11(b), an image, corresponding to only one of the gratings, can be acquired. In Fig. 11(c), the images for both light sources and gratings are depicted. As it is clearly visible for grating $G1$, a larger share of diffracted radiation is distributed in the x direction for LED as well as HeNe laser illumination. However, for grating $G2$, the vertical expansion in the X direction is reduced to the diameter of the entrance pinhole, which is the lower limit of this mount, as it is imaged nearly in a 1:1 ratio onto the detector plane. This is only surpassed by the HeNe laser which was focused into the pinhole so that the pinhole does not pose the field stop for the setup and a smaller focus spot is achievable. The cross sections of the focal spot images, depicted in the graphs in Fig. 11(d), further illustrate the suppression of X -axis astigmatism, as not only a smaller spot radius but also steeper ascent at the boundaries of the focal regions are achieved, which corresponds to the sharper imaging of the pinhole aperture.

Although the manufactured diffraction gratings are primarily presented with respect to their imaging properties, diffraction efficiency and interorder stray light are also of relevance, which are listed in Table 3. The reader is referred to Refs. 19 and 29 where the measurement setup and results are described in more detail.

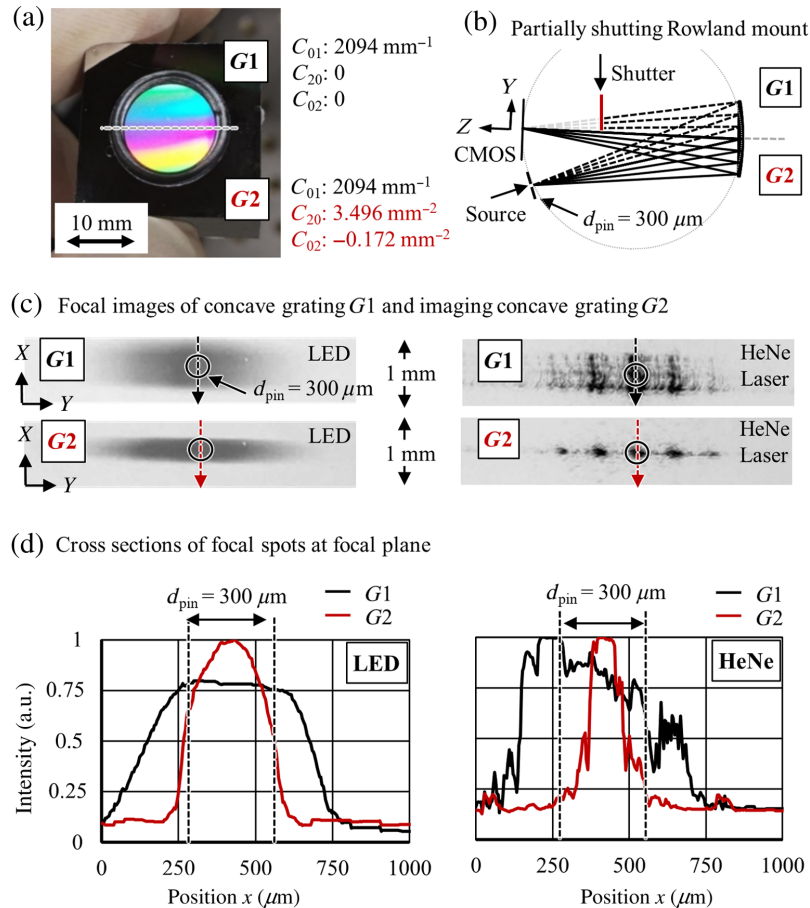


Fig. 11 (a) Photograph of a curved, diametrically divided diffraction grating with (G2) and without (G1) aberration correcting phase function coefficients. (b) Scheme of the testing setup which incorporates a shutter so that each diffractive surface can be individually probed. (c) CMOS detector images of the diffracted beams for each diffractive surface. (d) Cross sections along the vertical axis of the focal regions of the diffractive beams, depicting a significantly smaller spot size for the aberration-corrected surface (G2).¹⁹

Table 3 Optical performance of the manufactured gratings.

Parameter	Value
Flat gratings	
Straylight level (between first and zeroth diffraction order, normalized to the first-order peak intensity) ¹⁹	1.5E-4 to 2E-4
Curved grating	
RMS spot radius (raytracing)	7.79 μm
Straylight level (between first and zeroth diffraction order, normalized to the first-order peak intensity) ²⁹	1.3E-4
Diffraction efficiency (measured integrally over the grating surface, normalized to the theoretically achievable maximum diffraction efficiency) ²⁹	0.58

6 Conclusions and Outlook

This article describes the feasibility of the UP machining of flat and curved imaging gratings for aberration correction. It outlines a method for numerically calculating the trajectory programming based on the phase function and determining the machining parameters. The approach

involves the 2π -modulo-segmentation of the phase function of the grating into supporting points of the groove trajectories. This approach demands the consideration of the finite side-clearance angle of the used diamond tool. Steep incidence angles and/or low f -numbers potentially necessitate an axial rotation of the shaping diamond tool so that compromises regarding optical functionality and machining complexity have to be met through the collaboration of optics and manufacturing engineers. The applicability of the method and technology is demonstrated by flat and curved gratings with and without nonlinear phase functions. An imaging capability of flat samples is demonstrated as well as the aberration correction of a curved Rowland grating mount.

Comparable optical functionalities can be achieved in certain parameter ranges with other processes, e.g., IFL. However, machining by means of UP enables the manufacture of some geometries, particularly in the area of sharp-edged blaze structures, including echelle gratings, which cause high efforts in IFL manufacture. Aberration correction was previously mostly conducted on geometries that could be produced with IFL. Moreover, the production times for lithographic elements, excluding the actual illumination process, are usually in the region of weeks or months. Electron beam or mask-based lithography processes are difficult to implement on strongly curved surfaces. By contrast, the manufacturing times for the strongly curved gratings described in this article, including optics design, groove trajectory calculation, machine-tool setup, and the actual cutting process, are within a few days. The machining process is—within the described limits—nearly independent of the phase function of the grating. This allows for the production of varying and different gratings without significant modifications to the machine tool setup, which benefits prototypical or small-series production of diffractive imaging elements. The described method and process offer a way to partially overcome the restrictions of state-of-the-art grating production technologies in terms of groove dimensions, curvature, and production time, expanding the possibilities for manufacturing diffraction gratings.

Disclosures

The authors declare no conflicts of interest related to this work.

Code and Data Availability

The used code for the generation of the machine codes is available upon reasonable request from the corresponding author: m.jagodzinski@tu-berlin.de.

Acknowledgments

The machined diffraction gratings were made and used for the research project “Copysphär” (Grant No. 10169159), which was supervised by the Investment Bank Berlin (IBB) and financed through funds from the European Funds for Regional Development (EFRE). Special thanks to our colleagues of the Department for Nonlinear Optics, led by Ulrike Woggon, for the support with the numerical raytracing analyses with Zemax OpticStudio.

References

1. T. Glaser, “High-end spectroscopic diffraction gratings: design and manufacturing,” *Adv. Opt. Technol.* **4**(1), 25–46 (2015).
2. T. Harada and T. Kita, “Mechanically ruled aberration-corrected concave gratings,” *Appl. Opt.* **19**(23), 3987–3993 (1980).
3. T. Kita, T. Harada, and S. Moriyama, “Diffraction grating ruling engine,” US Patent US4219933A (1980).
4. J. M. Cobb et al., “Innovative manufacturing and test technologies for imaging hyperspectral spectrometers,” *Proc. SPIE* **6233**, 62330R (2006).
5. M. A. Davies et al., “Application of precision diamond machining to the manufacture of microphotonic components,” *Proc. SPIE* **5183**, 94–108 (2003).
6. R. Gläbe and O. Riemer, “Diamond machining of micro-optical components and structures,” *Proc. SPIE* **7716**, 771602 (2010).
7. E. Brinksmeier, O. Riemer, and R. M. Gläbe, *Fabrication of Complex Optical Components*, Springer Berlin Heidelberg (2013).

8. E. Brinksmeier et al., "Submicron functional surfaces generated by diamond machining," *CIRP Ann. Manuf. Technol.* **59**(1), 535–538 (2010).
9. E. Brinksmeier, R. Gläbe, and L. Schönemann, "Review on diamond-machining processes for the generation of functional surface structures," *CIRP J. Manuf. Sci. Technol.* **5**(1), 1–7 (2012).
10. E. Brinksmeier, R. Gläbe, and L. Schönemann, "Diamond micro chiseling of large-scale retroreflective arrays," *Precis. Eng.* **36**(4), 650–657 (2012).
11. E. Brinksmeier and L. Schönemann, "Generation of discontinuous microstructures by Diamond Micro Chiseling," *CIRP Ann. Manuf. Technol.* **63**(1), 49–52 (2014).
12. S. Kühne et al., "Fabrication and characterization of machined 3D diffractive optical elements," *Microsyst. Technol.* **20**(10), 2103–2107 (2014).
13. A. Gebhardt et al., "MERTIS: optics manufacturing and verification," *Proc. SPIE* **7808**, 78080Q (2010).
14. F. Niehaus, *Herstellung von diskontinuierlichen Mikrostrukturen durch Ultrapräzisionszerspanung*, Apprimus-Verlag, Aachen (2013).
15. M. A. Davies et al., "Diamond machining of diffraction gratings for imaging spectrometers," *Precis. Eng.* **36**(2), 334–338 (2012).
16. T. Moriya et al., "Creation of V-shaped microgrooves with flat-ends by 6-axis control ultraprecision machining," *CIRP Ann. Manuf. Technol.* **59**(1), 61–66 (2010).
17. Y. Takeuchi et al., "6-Axis control ultraprecision microgrooving on sculptured surfaces with non-rotational cutting tool," *CIRP Ann. Manuf. Technol.* **58**(1), 53–56 (2009).
18. S. Kühne, *Ultrapräzisionsverfahren zur Erhöhung der Güte abbildender Beugungsgitter*, from *Berichte aus dem Produktionstechnischen Zentrum Berlin*, Fraunhofer Verlag, Stuttgart (2018).
19. M. Jagodzinski, *Optimierung der optischen Eigenschaften diamantzerspanter Beugungsgitter mit mehreren Freiheitsgraden durch Minimierung der Maschinenkinematik*, from *Berichte aus dem Produktionstechnischen Zentrum Berlin*, Fraunhofer Verlag, Berlin (2022).
20. K. Haskic, *Verfahren zur mechanischen Erzeugung periodischer nanooptischer Strukturen mit monokristallinen Diamantwerkzeugen am Beispiel von Blazegittern*, from *Berichte aus dem Produktionstechnischen Zentrum Berlin*, Fraunhofer Verlag, Berlin (2015).
21. M. Jagodzinski et al., "Suitability of RSA aluminum for monolithic DOE in the VIS range," in *ASPE 33rd Annu. Meet.*, Las Vegas (2018).
22. F. Hölzel et al., "Reactive ion beam smoothing of rapidly solidified aluminum (RSA) 501 surfaces for potential visible and ultraviolet light applications," *Surf. Interfaces* **38**, 102784 (2023).
23. B. Borguet et al., "The dual-blazed diffraction grating of the CHIME hyperspectral instrument: design, modelling, and breadboarding," *Proc. SPIE* **12777**, 127772H (2023).
24. H. Noda, T. Namioka, and M. Seya, "Geometric theory of the grating," *J. Opt. Soc. Am.* **64**(8), 1031–1036 (1974).
25. H. Noda, T. Namioka, and M. Seya, "Design of holographic concave gratings for Seya-Namioka monochromators," *J. Opt. Soc. Am.* **64**(8), 1043–1048 (1974).
26. H. Noda, T. Namioka, and M. Seya, "Ray tracing through holographic gratings," *J. Opt. Soc. Am.* **64**(8), 1037–1042 (1974).
27. M. Jagodzinski et al., "New approaches in ultra precision manufacturing of diffraction gratings," in *Euspen Special Interest Group: Struct. & Freeform Surf. Virtual Special Interest Group Meet.*, October (2020).
28. T. Stone and N. George, "Hybrid diffractive-refractive lenses and achromats," *Appl. Opt.* **27**, 2960–2971 (1988).
29. M. Jagodzinski et al., "Minimization of kinematic complexity while diamond machining of curved diffraction gratings," in *Proc. EUSPEN 22nd Int. Conf. & Exhibit.*, Geneva (2022). <https://www.euspen.eu/knowledge-base/ICE22139.pdf>.

Marco Jagodzinski is a research assistant in the Micro and Precision Devices Department (MFG). He graduated in 2016 with an MSc degree and completed his PhD with "summa cum laude" in 2022, both in the realm of ultraprecision machining of diffractive optics. After a 1-year tenure in the field of Raman spectroscopy at the working group of Ulrike Woggon, he is now back at the MFG, working in the domain of textile sorting using computer vision artificial intelligence.

Stefan Kühne is the group leader in the Micro and Precision Devices Department. He graduated in 2010 with a diploma in precision mechanics and microtechnology and subsequently worked at HU Berlin (BCCN). Returning to TU Berlin in 2012, he completed his PhD in 2017 with "summa cum laude." Since 2013, he has been responsible for student lectures and demonstrating expertise in spectroscopy and microfluidic devices through extensive research and over 20 years of membership in the German Physical Society.

Dirk Oberschmidt studied mechanical engineering with a focus on manufacturing at FHTW Berlin and later earned a Diplom-Ingenieur in production technology at TU Dresden. During his doctoral studies, he worked at IWF and Fraunhofer IPK in Berlin, specializing in ultraprecision machining. For 12 years, he led the joint Microproduction Technology group of both institutions. Since 2018, he has been a professor of Micro and Precision Devices at TU Berlin.